Large second-harmonic generation and linear electro-optic effect in the bulk kagome lattice compound Nb_3MX_7 (M = Se, S, Te; X = I, Br)

Zhiwen Chen,[1] Yimei Fang,[1,*] Meijuan Cheng,[2] Tie-Yu Lü,[1] Xinrui Cao,[1,3] Zi-Zhong Zhu,[1,3] and Shunqing Wu[1,†]

[1]*Department of Physics, OSED, Key Laboratory of Low Dimensional Condensed Matter Physics (Department of Education of Fujian Province), Xiamen University, Xiamen 361005, China*

[2]*School of Science, Jimei University, Xiamen 361021, China*

[3]*Fujian Provincial Key Laboratory of Theoretical and Computational Chemistry, Xiamen University, Xiamen 361005, China*

(Received 18 November 2023; revised 13 February 2024; accepted 20 February 2024; published 11 March 2024)

Layered Nb_3MX_7 (M = Se, S, Te; X = I, Br) compounds with a noncentrosymmetric kagome lattice structure constitute a promising candidate for exhibiting optical anisotropy and nonlinearity. Nevertheless, there has been limited research on their nonlinear optical properties both theoretically and experimentally. In this paper, we systematically study the linear and nonlinear optical responses of the bulk Nb_3MX_7 (M = Se, S, Te; X = I, Br) family. Previously, two distinct stacking sequences (i.e., AA and AB stacking) in Nb_3MX_7 compounds had been identified in experiments. Therefore, the influence of the stacking sequence and the isoelectronic substitution on the linear and nonlinear optical response of the Nb_3MX_7 compounds are investigated. It reveals that all four materials (AB-Nb_3TeI_7, AA-Nb_3TeI_7, AB-Nb_3SeI_7, and AA-Nb_3SBr_7) exhibit significant second-harmonic generation and linear electro-optic effects. Notably, the second-harmonic generation coefficient ($\chi^{(2)}_{zzz}$) of AB-Nb_3TeI_7 reaches 3081 pm/V at 0.91 eV, which is nearly 14 times as large as that of the known nonlinear optical material GaN. Furthermore, AB-Nb_3TeI_7 exhibits a large linear electro-optic coefficient $r_{zzz}(0)$ of 5.94 pm/V, which outperforms that of GaN by almost tenfold. The prominent nonlinear optical responses observed in the Nb_3MX_7 compounds are attributed to the intralayer directional covalent bonding. Our findings indicate that the Nb_3MX_7 materials would have potential applications in nonlinear optical and linear electro-optic devices.

DOI: 10.1103/PhysRevB.109.115118

I. INTRODUCTION

Nonlinear optical (NLO) responses, which originate in intense optical field-matter interactions, constitute an effective method to modulate the frequency and amplitude of incident electro-magnetic waves [1,2]. Franken and his co-workers' seminal work in 1961, which demonstrated the second-harmonic generation (SHG) experimentally for the first time, is widely regarded as the advent of modern nonlinear optics [3]. Theoretical investigations of SHG in semiconductors were promoted by the pioneering work of Sipe and Pedersen and their coworkers [4–7]. Since then, extensive efforts have been dedicated to exploring SHG in bulk semiconductors [8–12] and two-dimensional [13–17] and one-dimensional materials [18–20]. The process of SHG is known for its remarkable efficiency, as it can achieve near-complete conversion of the incident beam's power at frequency ω into radiation at the second-harmonic frequency 2ω, given the appropriate experimental conditions. Therefore, SHG materials exhibit great potential for applications in lasers and frequency converters [21–23]. Another second-order NLO phenomenon is the linear electro-optical (LEO) effect, which measures the changes of refractive index (Δn) induced by an electric field in a medium. By controlling the electric signals, the LEO effect enables the manipulation of the amplitude, phase, and propagation direction of optical beams in NLO materials [24].

Recent years have witnessed a growing interest in second-order NLO research of two-dimensional (2D) layered materials, especially the transition metal dichalcogenides (TMDCs). The SHG in MoS_2, a representative of TMDCs, has been extensively studied both experimentally and theoretically [25–29]. These studies have revealed that the SHG coefficients of monolayer MoS_2 can reach magnitudes on the order of 1000 pm/V [25,26,29], a significant enhancement compared to the value of ~0.01 pm/V [28] for bulk MoS_2. Further investigations have been extended to other MX_2 (M = Mo, W; X = S, Se, Te) [30–33]. Similar layer-dependent behavior in SHG has been observed in these 2D hexagonal TMDCs, where giant SHG signals are present in odd layers due to broken symmetry, while SHG is vanished in even layers with restored inversion symmetry. An intriguing study by Guo *et al.* [34] demonstrated that 2D pentagonal PdX_2 (X = S, Se) also exhibit layer-dependent SHG, with SHG observed in even layers. This is attributed to the noncentrosymmetric nature of even-layer PdX_2, in contrast to the centrosymmetric odd-layer PdX_2. While significant SHG effects are found in odd layers of hexagonal TMDCs or even layers of pentagonal TMDCs, their bulk counterparts do not display notable nonlinear optical (NLO) responses due to the recovery of spatial inversion symmetry in the bulk phases.

In contrast, the layered kagome semiconductors may be noncentrosymmetric even in their bulk form [35–37]. Since

*ymfang@xmu.edu.cn
†wsq@xmu.edu.cn

their discovery, kagome semiconductors have attracted considerable attention due to their unique properties, such as a high degree of anisotropy, broken inversion symmetry, and topological flat bands [35,36,38]. The kagome semiconductor Nb_3I_8 has a layered CdI_2 structure, with Nb atoms occupying triangles capped by I ions. Substituting the lower electronegativity chalcogen ions (S, Se, Te) for the electron-deficient capping I ions produces Nb_3MI_7 (M = S, Se, Te), which enlarges the dipole moments with respect to Nb_3I in the Nb_3X tetrahedra. This leads to the formation of electronically distinct Nb_3 clusters. Besides, the residual I ions can also be replaced by other halogen elements, significantly expanding the Nb_3MX_7 family.

The bulk Nb_3MX_7 (M = S, Se, Te; X = Br, I) materials, as noncentrosymmetric semiconductors, exhibit two primary second-order nonlinear optical responses, namely, SHG and the LEO effect. However, the linear and nonlinear optical properties of these materials have been scarcely studied. Only SHG signals have been reported for the Nb_3SeI_7 nanoflake [37,39]. For this reason, we perform systematic *ab initio* calculations to study the linear and nonlinear optical properties of the Nb_3MX_7 materials. From the computed dielectric function and dipole transitions, we can also gain better understanding of the SHG and LEO coefficients. It would be helpful in investigating the NLO properties of these fascinating layered kagome lattice materials.

The paper is organized as follows. Section II introduces the computational and theoretical details. Section III presents the optical dielectric functions, SHG, and LEO coefficients of the Nb_3MX_7 materials. The influence of the stacking sequence and the isoelectronic substitution on the dielectric functions and SHG susceptibilities are discussed. The features of the NLO spectra are analyzed according to the interband and intraband single- and two-photon resonances. Finally, Sec. IV provides the conclusions of this work.

II. COMPUTATIONAL METHODS

All the optical calculations are performed utilizing the ABINIT [40,41] package. To ensure the convergences of the second-order susceptibilities, we adopt a k-point mesh of $2\pi \times 0.02$ Å^{-1} [42] with a plane-wave energy cutoff of 35 Ha, and the number of bands is set to be 330 and 220 for AB- and AA-Nb_3MX_7 Nb_3MX_7, respectively. Structural relaxation is conducted until forces on each atom are smaller than 0.001 eV/Å. The Perdew-Burke-Ernzerhof (PBE) functional [43] was utilized along with Grimme's D2 empirical correction [44] to account for the London dispersion, which is significant in van der Waals layered materials. Using the methodologies and formulations developed by Sipe *et al.* [5,45], we compute the linear and nonlinear susceptibility tensors for the Nb_3MX_7 materials.

Within the framework of linear response theory, the polarization is characterized by the following relation to the electric field [45]:

$$P^j(\omega) = \chi^{(1)}_{jl}(-\omega, \omega)E^l(\omega), \tag{1}$$

where $\chi^{(1)}_{jl}(-\omega, \omega)$ represents the jlth component of the complex dielectric tensor, j and l denote Cartesian directions, and $E^l(\omega)$ denotes the l component of the electric field at frequency ω. The linear optical response originates from the complex linear susceptibility tensor $\chi^{(1)}_{jl}(-\omega, \omega)$, which for semiconductors is given by [5] ($\hbar = m = e = 1$):

$$\chi^{(1)}_{jl}(-\omega, \omega) = \frac{1}{\Omega}\sum_{nm\boldsymbol{k}} f_{nm}\frac{r^j_{nm}(\boldsymbol{k})r^l_{mn}(\boldsymbol{k})}{\omega_{mn}(\boldsymbol{k}) - \omega} = \frac{\varepsilon_{\mathrm{jl}}(\omega) - \delta_{\mathrm{jl}}}{4\pi}. \tag{2}$$

In Eq. (2) and content that follows, m and n are the band label; ε_0 is the permittivity of free space; Ω is the volume of the unit cell. $f_{nm} = f_n - f_m$ is the difference of Fermi occupations, where f_n is the Fermi occupation of band n. ω_{mn} is the frequency difference between bands m and n. Here the vectors $\boldsymbol{k}$ range over the Brillouin zone, and r_{nm} are the position matrix elements. $\varepsilon_{jl}(\omega)$ is the jlth component of the dielectric function. The complex dielectric function possesses both a real component and an imaginary component. The $\mathrm{Re}[\varepsilon_{jl}(\omega)]$ can be obtained from the computed $\mathrm{Im}[\varepsilon_{2,jl}(\omega)]$ via Kramers-Kronig transformation.

For the second-order response, the nonlinear polarization component can be written as follows with the electric field by

$$P^j(\omega_\beta + \omega_\gamma) = \chi^{(2)}_{jkl}(-\omega_\beta - \omega_\gamma, \omega_\beta, \omega_\gamma)E^k(\omega_\beta)E^l(\omega_\gamma). \tag{3}$$

The derivation of the second-order susceptibility $\chi^{(2)}_{jkl}$ uses the methods of Sipe *et al.* [5,45]. During the SHG process, the system absorbs two photons, each with energy $\hbar\omega$, resulting in the emission of a photon with doubled energy $2\hbar\omega$. Given that $\omega_\beta = \omega_\gamma$ in this process, the frequency-dependent second-order susceptibility specific to SHG is expressed as $\chi^{(2)}_{jkl}(-2\omega, \omega, \omega)$ or more succinctly $\chi^{(2)}(2\omega)$. Within ABINIT [46], the nonlinear susceptibility of SHG is computed as the sum of three distinct contributions, according to the following relation:

$$\chi^{(2)}_{jkl}(2\omega) = \chi^{II}_{jkl}(2\omega) + \eta^{II}_{jkl}(2\omega) + \frac{i}{2\omega}\sigma^{II}_{jkl}(2\omega). \tag{4}$$

Equation (4) describes three distinct contributions to the second-order susceptibility. The first term $\chi^{II}_{jkl}(2\omega)$ represents the role of interband transitions, illustrating how electrons moving between different energy bands contribute to the nonlinear optical response. The second term $\chi^{II}_{jkl}(2\omega)$ captures the influence of electrons' intraband movements on the linear susceptibility, essentially showing how the motion within the same energy band modulates the material's response to light. The final term describes the impact of polarization energy and interband movements on modifying the susceptibility. A detailed examination and discussion of these contributions have been previously presented [5].

For the linear electro-optic response, a single incident photon of energy $\hbar\omega$ (generating a time-varying electric field) is incident on the material, with an electric potential also applied to the material. Considering the electric field displacement vector, the measurable Pockels coefficient can be related to the linear electro-optic susceptibility. This relationship can be simplified and expressed as the effective dielectric function multiplied by the electric field, describing the first-order relationship between a constant electric field and the change in the system's inverse effective dielectric function, i.e., the Pockels

TABLE I. Lattice constants and band gaps of the Nb_3MX_7 family. Experimental values are shown in parentheses. The scissors operator is defined as $\Delta E = E_g^{(\mathrm{HSE+SOC})} - E_g^{(\mathrm{GGA+SOC})}$, where $E_g^{(\mathrm{HSE+SOC})}$ and $E_g^{(\mathrm{GGA+SOC})}$ are the SOC band gaps calculated at the HSE and GGA levels, respectively.

	a (Å)	c (Å)	$E_g^{(\mathrm{GGA+SOC})}$ (eV)	$E_g^{(\mathrm{HSE+SOC})}$ (eV)	ΔE (eV)
AB-Nb_3TeI_7	7.604 (7.630 [35])	13.653 (13.800 [35])	0.430	1.096	0.666
AA-Nb_3TeI_7	7.613 (7.642 [35])	6.801 (6.897 [35])	0.364	1.042	0.678
AA-Nb_3SBr_7	7.086 (7.642 [56])	6.258 (6.304 [56])	0.764	1.667	0.903
AB-Nb_3SeI_7	7.551 (7.594 [37])	13.391 (13.655 [37])	0.446	1.153 (1.54 [37])	0.707

coefficient. Thus, the LEO coefficient is written as

$$r_{jkl}(\omega) = \frac{-2\chi_{jkl}^{EO}(\omega, \omega, 0)}{(\eta_{jj}(\omega)n_{kk}(\omega))^2}. \quad (5)$$

It is known that the band gaps of semiconductors are usually underestimated by the PBE functional within the generalized gradient approximation, where quasiparticle self-energy corrections are not appropriately accounted for. To improve the accuracy, various hybrid exchange-correlation functionals, such as B3PW and B3LYP functionals [47,48], and the Heyd-Scuseria-Ernzerhof (HSE) hybrid functional [49,50], have been developed. These methods have been reported to yield band gap values that are in better agreement with experimental measurements [51–54].

An accurate band gap is crucial for obtaining accurate optical properties. Therefore, we further perform band structure calculations using the HSE functional to improve the description of band gaps of the Nb_3MI_7 (M = S, Se, Te) family. Subsequently, the band gaps obtained by the HSE calculations are utilized and the self-energy corrections are taken into account via the so-called scissor correction [54]. In the scissor correction calculations, the conduction bands are rigidly shifted upwards to fit the HSE band gap, and the transition matrix elements are modified correspondingly. All the optical properties presented in this paper are obtained with the scissor correction.

III. RESULTS AND DISCUSSION

A. Crystal structure and electronic properties

The layered noncentrosymmetric Nb_3MX_7 (M = Te, Se, S; X = Br, I) materials were synthesized in experiments [35–37] and were found to exhibit polymorphism. Two polymorphs which differ in layer stacking sequences are determined [35]. We refer to them as AA-Nb_3MX_7 Nb_3MX_7 and AB-Nb_3MX_7. Both structures crystallize in hexagonal lattices while having a different space group of $P6_3mc$ and $P3m1$, respectively. As illustrated in Fig. 1, both polymorphs consist of [Nb_3MX_7 slabs separated by Van der Waals gaps. Each [Nb_3MX_7] slab is composed of one pure iodide layer, one mixed "M/X" layer, and one sandwiched Nb_3 trimer layer. In AA-Nb_3MX_7, the [Nb_3MX_7] slabs are directly superimposed on top of each other. For AB-Nb_3MX_7, the two adjacent [Nb_3MX_7] slabs are related by a 6_3 screw axis. Both AA- and AB-stacked configurations lack an inversion center, therefore they hold broken spatial inversion symmetry. The calculated and experimentally measured structural parameters of the AB-stacked Nb_3SeI_7 and Nb_3TeI_7, and the AA stacked-Nb_3SBr_7 and Nb_3TeI_7 are listed in Table I. The optimized atomic coordinates of the four Nb_3MX_7 (M = Te, Se, S; X = Br, I) materials can be found in Table S1 in the Supplemental Material [55]. The differences between the optimized lattice constants and the experimental measurements are within 2% for all four compounds.

Since Nb_3MX_7 compounds share the same crystal structure and their constituent elements fall into the same groups in the periodic table, the band structures are quite similar among the Nb_3MX_7 family. Here we show only the band structure of the AB-stacked Nb_3TeI_7 in Fig. 2(a). The band structure of AA-Nb_3TeI_7, AB-Nb_3SeI_7, and AA-Nb_3SBr_7 can be found in Figs. S1(a), S1(c), and S1(e). Both AA- and AB-stacked Nb_3MX_7 are direct band-gap semiconductors with both the conduction band minimum (CBM) and valence band maximum (VBM) locating at the Γ point. The band gaps for the Nb_3MX_7 family obtained at the PBE and HSE levels with the spin-orbit coupling (SOC) effect taken into account are

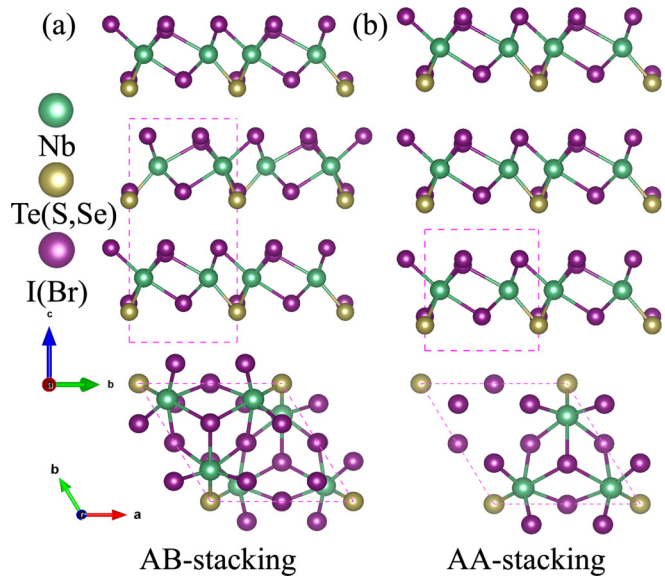

FIG. 1. Crystal structure of (a) AB-Nb_3MI_7 (M = Te, Se), (b) AA-Nb_3MX_7 (M = Te, Se; X = I, Br). Magenta dashed lines represent the unit cell.

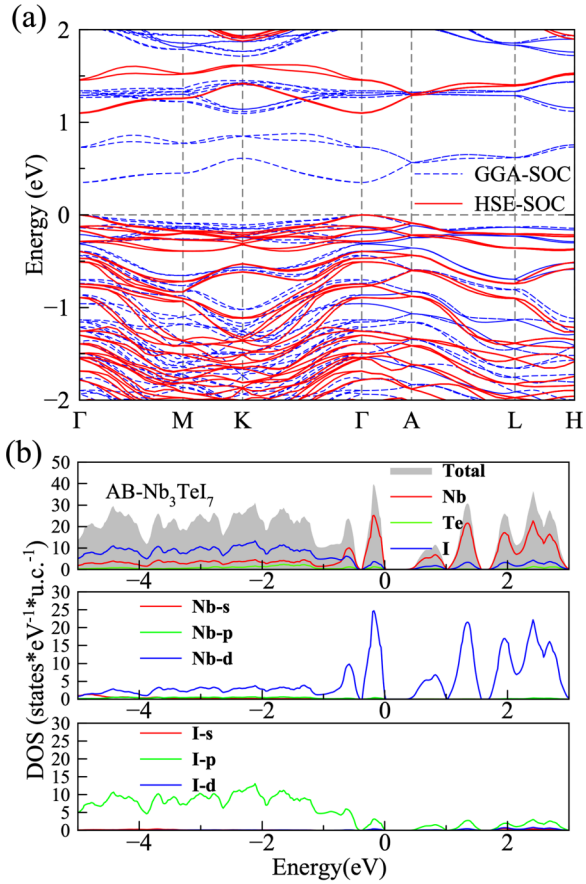

FIG. 2. (a) Band structures from GGA (blue dashed lines) and HSE (red solid lines) calculations. The horizontal dashed line denotes the Fermi level. (b) Total and orbital-projected DOS of AB-Nb_3TeI_7. Total and atom-projected DOS of AB-Nb_3TeI_7 are shown in the upper panel. The orbital-resolved DOS of Nb and I atoms are shown in the medium and bottom panels, respectively.

tabulated in Table I. The HSE functional greatly improves the description of band gaps of the Nb_3MX_7 family. For AB-Nb_3SeI_7, the PBE functional predicts a band gap of 0.446 eV, while the HSE functional gives 1.153 eV, which approaches the experimental value of 1.54 eV [37]. The band gap differences between the PBE and HSE levels are utilized to apply scissor corrections for more accurate estimation of the optical properties.

The total and orbital projected density of states (DOS) from PBE functional for all compounds are shown in Fig. 2(b) and Figs. S1(b), S1(d), and S1(f). Since the four compounds share rather similar DOS profile, here we focus only on the DOS of AB-Nb_3TeI_7. As shown in Fig. 2(b), the low-energy region from −5 to −1 eV is primarily contributed by the I p orbitals. The upper valence bands and lower conduction bands are mainly contributed by Nb d orbitals and I p orbitals. Hence, the Nb 4d orbitals and I p orbitals would play the primary role in determining the linear and nonlinear optical responses of the Nb_3MX_7 compounds.

B. Linear optical properties

The imaginary (absorptive) and real part of the optical dielectric function $\varepsilon(\omega)$ of Nb_3MX_7 is shown in Fig. 3 and

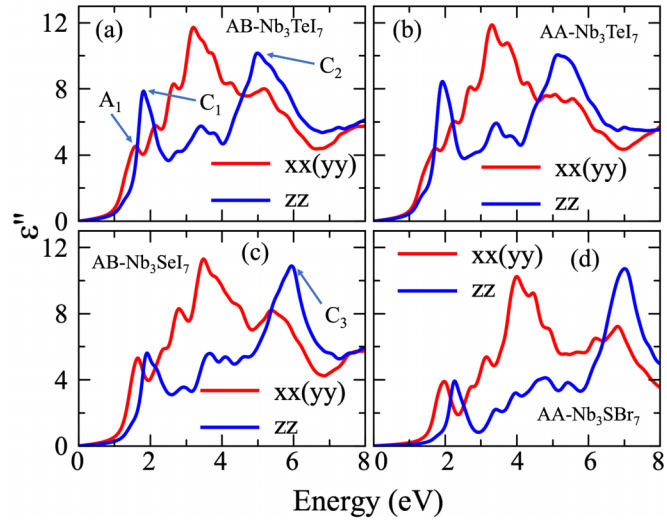

FIG. 3. Absorptive part of the optical dielectric function $\varepsilon''(\omega)$ of (a) AB − Nb_3TeI_7, (b) AA-Nb_3TeI_7, (c) AB-Nb_3SeI_7, and (d) AA-Nb_3SBr_7 for light polarization along the x(y) directions (red lines) and the z direction (blue lines). A_1 presents the first peak in the x(y) direction; C_1, C_2, and C_3 present peaks in the z direction.

Fig. S2, respectively. Due to the hexagonal symmetry, the two in-plane components (ε''_{xx} and ε''_{yy}) of the dielectric functions are equal. However, there is significant difference between the in-plane and out-of-plane components of the dielectric functions. As shown in Fig. 3(a) for AB-Nb_3TeI_7, the in-plane ε''_{xx} and ε''_{yy} doubles the out-of-plane ε''_{zz} in the energy range from 2.2 eV to 4.5 eV, while ε''_{zz} becomes slightly larger than ε''_{xx} and ε''_{yy} in the higher energy 5 eV region. By comparing the imaginary dielectric functions of AB-Nb_3TeI_7 and AA-Nb_3TeI_7 [see Fig. 3(a) and Fig. 3(b)], we find that the absorptive spectrum is hardly affected by the stacking sequence. Fig. 3(a) and Fig. 3(c) show that while the imaginary dielectric functions of AB-Nb_3TeI_7 and AB-Nb_3SeI_7 are similar, substituting Se for Te weakens the out-of-plane C_1 peak at ∼2 eV and leads to blue shifting of the higher energy absorption peaks. In contrast, the highest ε''_{zz} peak (C_2) is enhanced when Te is replaced with Se. Blue shift of C_2 peak is also observed, suggesting that the absorption of deeper UV radiation is improved in AB-Nb_3SeI_7.

When simultaneously replacing Te and I in AA-Nb_3TeI_7 with lighter S and Br atoms, a more pronounced shoulder peak near 5 eV occurs in the in-plane ε''_{xx} and ε''_{yy}; see Fig. 3(d). Additionally, the first peak of ε''_{xx} and ε''_{yy} is broadened, and the absorption peaks of ε''_{zz} are blue shifted with the first peak weakened and the strongest peak enhanced.

To better understand the origins of the main peaks, we employed the irvsp [57] code to identify the symmetries of low-energy bands at the Γ point, and assigned the main absorption peaks to interband transitions according to the dipole selection rules [58] tabulated in Table II. As depicted in Fig. 4, the first absorptive peak in the dielectric function as indicated as A_1 in Fig. 3(a) is related to the transitions from the Γ_6 state at the top of the valence band to the Γ_4 state at ∼1.6 eV. The out-of-plane C_1 peak can be assigned to the transitions from

TABLE II. Dipole selection rules [58] for transitions between the band states of C_{6v} group at the Γ point.

	E⊥c	**E**||**c**
Γ	$\Gamma_1 \to \Gamma_6$	$\Gamma_1 \to \Gamma_1$
	$\Gamma_6 \to \Gamma_1$	$\Gamma_2 \to \Gamma_2$

the Γ_1 state of valence band at −0.542 eV to the Γ_1 state of conduction band at 1.218 eV.

C. Second harmonic generation and linear electro-optic effect

The point group C_{6v} has four nonvanishing second-order nonlinear optical susceptibility elements [1]. Bulk AB-stacked Nb_3MX_7 compounds have C_{6v}^4 crystalline symmetry, which reduces the original number of nonzero elements by one because $\chi^{(2)}_{xxz} = \chi^{(2)}_{xzx} = \chi^{(2)}_{yzy} = \chi^{(2)}_{yyz}$. Thus, the AB-stacked Nb_3MX_7 have three nonzero SHG tensor elements, namely, $\chi^{(2)}_{xxz}$, $\chi^{(2)}_{zxx}$, and $\chi^{(2)}_{zzz}$. The AA-stacked Nb_3MX_7 have C_{3v}^1 crystalline symmetry and four nonzero SHG elements, $\chi^{(2)}_{xxz}$, $\chi^{(2)}_{yyy}$, $\chi^{(2)}_{zxx}$, and $\chi^{(2)}_{zzz}$. We note that the profiles of the NLO spectra remain nearly unaltered under the scissor correction, hence only the postscissor correction NLO spectra are presented in Fig. 5. However, the peak positions exhibit blue shifts, and the magnitudes of the second-order susceptibilities are reduced under the scissor correction.

In Table III the computed static dielectric constant $\varepsilon(0)$, second-order nonlinear optical susceptibility $\chi^{(2)}(0, 0, 0)$, and zero-frequency LEO coefficient $r(0)$ are listed. All the Nb_3MX_7 compounds show anisotropic behavior in both static second-order NLO susceptibilities and LEO coefficients. In addition, they all exhibit large static second-order NLO susceptibilities, especially $\chi^{(2)}_{zzz}(0)$, which are approximately 30 times that of the zincblende and wurtzite GaN (∼10 pm/V) [9,11,59], the common used NLO semiconductors. The AB-Nb_3TeI_7 has the largest LEO coefficient $r_{zzz}(0)$ of 5.94 pm/V, being approximately 10 times larger than that of bulk GaN polytypes(∼0.6 pm/V) [9,11,59]. The real and imaginary

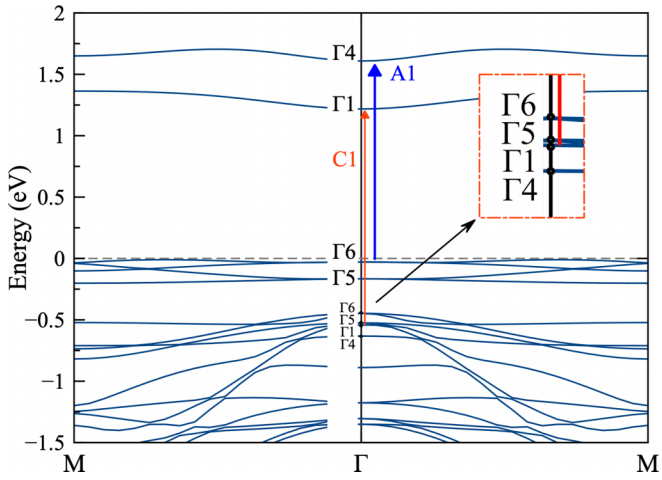

FIG. 4. Band structure of AB-Nb_3TeI_7 from GGA calculations with the scissor's correction. Red arrow denotes light polarization parallel to the *c* axis, blue arrow for perpendicular.

TABLE III. Static dielectric constants ($\varepsilon_x = \varepsilon_y, \varepsilon_z$), second-order susceptibilities $\chi^{(2)}(0)$(pm/V), and LEO coefficients $r(0)$(pm/V) for the bulk Nb_3MX_7 compounds.

	AB − Nb_3TeI_7	AA − Nb_3TeI_7	AB − Nb_3SeI_7	AA − Nb_3SBr_7
ε_x	10.86	10.72	10.62	8.29
ε_z	9.46	9.50	8.52	6.36
$\chi^{(2)}_{xxz}(0)$	−47.09	−39.60	−39.93	17.62
$\chi^{(2)}_{yyy}(0)$		82.51		60.55
$\chi^{(2)}_{zxx}(0)$	−43.29	−37.53	−39.91	25.51
$\chi^{(2)}_{zzz}(0)$	350.19	298.26	229.93	−111.07
$r_{xxz}(0)$	0.80	0.69	0.71	−0.51
$r_{yyy}(0)$		−1.43		−1.76
$r_{zxx}(0)$	0.73	0.65	0.71	−0.74
$r_{zzz}(0)$	−5.94	−5.19	−4.07	3.23

parts of the second-order susceptibility are shown in Fig. 5 for AB-Nb_3TeI_7 and Fig. S5 for AA-Nb_3TeI_7, AB-Nb_3SeI_7, and AA-Nb_3SBr_7, respectively. For all four compounds, $\chi^{(2)}_{zzz}$ is the dominant component of $\chi^{(2)}$. The $\chi^{(2)}_{zzz}$ of AB-Nb_3TeI_7 has the strongest response at 0.91 eV, which reaches 3081 pm/V, being an order of magnitude larger than that of gallium arsenide (GaAs) [60], nearly 14 times that of GaN (∼220 pm/V) [9,11,59], and almost 40 times that of the CdSe (∼76 pm/V) [61]. This indicates that AB-Nb_3TeI_7 would be an excellent NLO material, with potential applications in nonlinear and electro-optic optical devices, such as frequency conversion, optical switches, frequency doubling, optical modulation, and sensors [62,63].

We also examine the effect of stacking sequence on the NLO properties of the Nb_3MX_7 compounds. The comparison between the second-order susceptibilities of AB-Nb_3TeI_7 (Fig. 5) and AA-Nb_3TeI_7 [Fig. S3(a)] show the two stackings have rather similar profiles of $\chi^{(2)}_{xxz}$, $\chi^{(2)}_{zxx}$, and $\chi^{(2)}_{zzz}$. The only difference is that the intensities of the peaks at ∼4 eV of AB-Nb_3TeI_7 are weaker than that of AA-Nb_3TeI_7. This implies that the interlayer Van der Waals interactions have only negligible influence on the SHG. A comparison of AB-Nb_3SeI_7 [Fig. S3(b)] and AB-Nb_3TeI_7 (Fig. 5), which share the same stacking sequence but consist of different *M* elements, is drawn to demonstrate the impact of electronic substitution on the NLO properties. Similar to the case of linear dielectric function, the two compounds exhibit analogous features in the second harmonic response especially in the low-energy zone (<1.5 eV). This phenomenon can be attributed to the dominant contributions from Nb and I atoms near the Fermi level in the density of states, which primarily determine the second harmonic generation.

There are few studies on the NLO properties of the bulk Nb_3MX_7 compounds. Only experimental SHG intensity of the AB-Nb_3SeI_7 [37,39] nanoflake is available. Our computational findings are compared against the reported experimental values therein. In Fig. S4 the experimental results [37] show that AB-Nb_3SeI_7 exhibits a robust SHG response peak at 430 nm (∼2.9 eV). In our calculations, the response peak occurs at 2.5 eV with a magnitude of 500 pm/V. The discrepancy of peak position may arise from the difference between the HSE06 calculated band gap and the experimentally measured

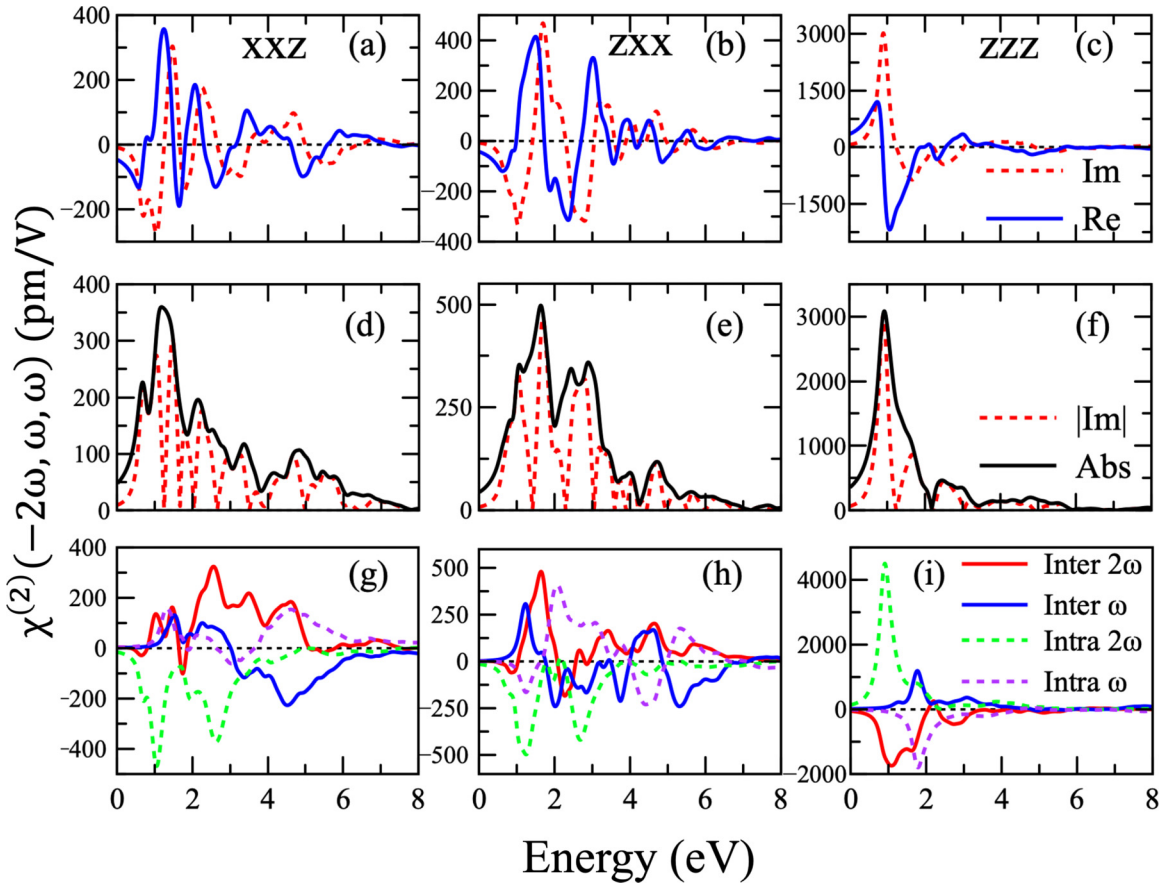

FIG. 5. (a–c) Real and imaginary parts, and (d–f) the absolute value of the second-order susceptibility of $\chi^{(2)}_{xxz}$, $\chi^{(2)}_{zxx}$, and $\chi^{(2)}_{zzz}$ of AB-Nb_3TeI_7. (g–i) Decomposition of the imaginary parts of $\chi^{(2)}_{xxz}$, $\chi^{(2)}_{zxx}$, and $\chi^{(2)}_{zzz}$ into the inter- and intraband single- and two-photon contributions, respectively.

band gap. Despite the band gap deviation, our computational results are in reasonable agreement with the experimental measurements.

The SHG involves not only single-photon resonances, but also two-photon resonances. To gain a deeper understanding of the NLO response, we analyze the constituent components of the second-order susceptibility to identify the key features in the spectra. The SHG spectrum can be decomposed into four parts, i.e., the interband and intraband single- and two-photon resonances. Since the $\chi^{(2)}_{zzz}$ component of $\chi^{(2)}$ of AB-Nb_3TeI_7 exhibits the maximum response peak among the four Nb_3MX_7 compounds investigated here, we focus on the discussion on the origins of the large $\chi^{(2)}_{zzz}$ in the AB-Nb_3TeI_7. Figures 5(d) and 5(g) depict the absolute values of $\chi^{(2)}$ and absolute values of the imaginary part of $\chi^{(2)}$, as well as the decompositions of $\chi^{(2)}$ of AB-Nb_3TeI_7. It is shown that the strongest peak of $\chi^{(2)}_{zzz}$ at 0.91 eV stems from the positive peak in the imaginary part of the $\chi^{(2)}_{zzz}$, which is dominated by intraband two-photon resonance. The interband two-photon resonance plays a secondary role in determining the highest peak of $\chi^{(2)}_{zzz}$, which shows opposite sign to intraband two-photon resonance.

Interestingly, for these four materials, as shown in Figs. 5(g), 5(h), and 5(i), and Fig. S3, in the energy range from approximately 0 to 2eV, the spectral features in the nonlinear optical response are formed predominantly by two-photon (2ω) resonances. $\chi^{(2)}_{zzz}$ is greater than those of $\chi^{(2)}$ components, from the real part, imaginary part, or magnitude perspectives. This can be attributed to the layered structure of these materials, which show significant in-plane and out-of-plane anisotropy.

To explore other origins of large SHG susceptibility in the Nb_3MX_7 family, the deformation charge density, which is defined as the difference between the total charge density and the superposition of spherical atomic charge densities, is depicted in Fig. 6. The analysis of the deformation charge density reveals a substantial accumulation of electron charge near the Nb-I and Nb-Te (Nb-Se) bond centers, while the charge is depleted from Nb along the bond directions. This indicates strong directional covalent bonding within the layers of these materials, which gives rise to significant spatial wavefunction overlap between initial and final states and, consequently, to large optical matrix elements and large $\chi^{(2)}$ values. Generally, a strong directional covalent bond is regarded as one of the major sources to produce significant SHG susceptibility, as is demonstrated in Refs. [20,34,64,65].

IV. CONCLUSION

We have systematically investigated the linear and NLO properties of the bulk Nb_3MX_7 (M = S, Se, Te; X = Br,

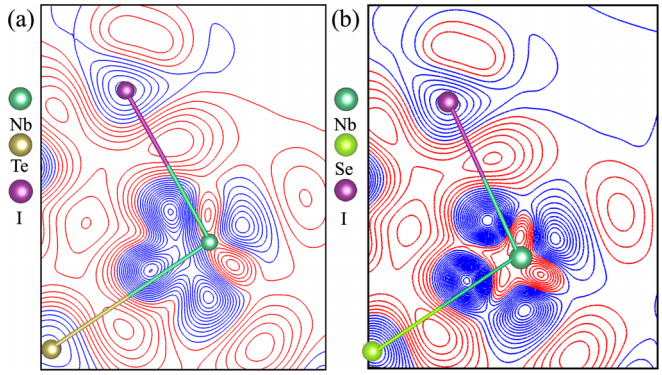

FIG. 6. Contour plot of the deformation charge density of (a)AB-Nb_3TeI_7 and (b)AB-Nb_3SeI_7 from GGA calculations. The contour interval is 0.002 eV/Å^3. The electron accumulation is denoted by red lines; the electron depletion is depicted by blue lines.

I) compounds, which possess a noncentrosymmetric layered Van der Waals kagome lattice. The Nb_3MX_7 family exhibits large second harmonic effects. Among the four compounds investigated here, the AB-stacked Nb_3TeI_7 has the strongest nonlinear optical susceptibility of 3081 pm/V in $\chi^{(2)}_{zzz}$, being approximately 14 times larger than that of the commonly utilized nonlinear optical material GaN and 40 times as large as that of CdSe. The strongest peak in the spectra of $\chi^{(2)}_{zzz}(-2\omega, \omega, \omega)$ is dominated by the intraband two-photon resonances. The AB-Nb_3TeI_7 exhibits gigantic static second harmonic generation coefficients, with the $\chi^{(2)}_{zzz}(0)$ (350 pm/V) being up to 30 times larger than that of GaN. It also possesses a large linear electro-optic coefficient $r_{zzz}(0)$ (5.94 pm/V) which is over ten times greater than that of GaN polytypes. Hence, AB-Nb_3TeI_7 constitutes an outstanding nonlinear optical material and may find valuable applications in nonlinear and electro-optic devices such as electro-optical switches, frequency converters, phase matchers, and optical signal modulators.

We also found that the stacking pattern has negligible impact on the dielectric functions and SHG in low-energy zone. The isoelectronic substitution of lighter elements for Te, i.e., replacing Te with Se or S, weakens the intensities of the low-energy absorptive peak but enhances and blue-shifts the high-energy absorption peak. However, the isoelectronic substitution does not significantly affect the spectral profiles of Nb_3MI_7 (M = Se, Te), as the optical properties are primarily determined by the energy states near the Fermi level, which are dominated by Nb and the group VIIA elements.

Recently, growing experimental effort has been paid to measure the NLO properties and the topological flat bands of two-dimensional Nb_3MX_7 compounds [66]. Our findings here will stimulate further experimental efforts on the nonlinear and electro-optic effects in bulk Nb_3MX_7 compounds, the parent materials of the 2D Nb_3MX_7.

ACKNOWLEDGMENTS

Work at Xiamen University was supported by the Fundamental Research Funds for the Central Universities (Grant No. 20720210023). S. Fang and T. Wu from the Information and Network Center of Xiamen University are acknowledged for their help with GPU computing. Work at Jimei University was supported by the National Natural Science Foundation of China Grant No. 12304083.

[1] Y. R. Shen, *The Principles of Nonlinear Optics*, Wiley Classics Library Edition (Wiley-Interscience, Hoboken, NJ, 2003).
[2] R. W. Boyd, *Nonlinear Optics*, 4th ed. (Academic Press, San Diego, 2019).
[3] P. A. Franken, A. E. Hill, C. W. Peters, and G. Weinreich, Generation of optical harmonics, Phys. Rev. Lett. **7**, 118 (1961).
[4] R. W. Boyd and J. E. Sipe, Nonlinear optical susceptibilities of layered composite materials, J. Opt. Soc. Am. B **11**, 297 (1994).
[5] J. L. P. Hughes and J. E. Sipe, Calculation of second-order optical response in semiconductors, Phys. Rev. B **53**, 10751 (1996).
[6] J. E. Sipe and R. W. Boyd, Nonlinear susceptibility of composite optical materials in the Maxwell Garnett model, Phys. Rev. A **46**, 1614 (1992).
[7] T. G. Pedersen, K. Pedersen, and T. Brun Kriestensen, Optical matrix elements in tight-binding calculations, Phys. Rev. B **63**, 201101 (2001).
[8] R. K. Chang, J. Ducuing, and N. Bloembergen, Dispersion of the optical nonlinearity in semiconductors, Phys. Rev. Lett. **15**, 415 (1965).
[9] V. I. Gavrilenko and R. Q. Wu, Linear and nonlinear optical properties of group-III nitrides, Phys. Rev. B **61**, 2632 (2000).
[10] C. Hu, M. Mutailipu, Y. Wang, F. Guo, Z. Yang, and S. Pan, The activity of lone pair contributing to SHG response in bismuth borates: A combination investigation from experiment and DFT calculation, Phys. Chem. Chem. Phys. **19**, 25270 (2017).
[11] D. Cai and G.-Y. Guo, Tuning linear and nonlinear optical properties of wurtzite GaN by c-axial stress, J. Phys. Appl. Phys. **42**, 185107 (2009).
[12] C. C. Stoumpos, L. Frazer, D. J. Clark, Y. S. Kim, S. H. Rhim, A. J. Freeman, J. B. Ketterson, J. I. Jang, and M. G. Kanatzidis, Hybrid germanium iodide perovskite semiconductors: Active lone pairs, structural distortions, direct and indirect energy gaps, and strong nonlinear optical properties, J. Am. Chem. Soc. **137**, 6804 (2015).
[13] L. Hu, X. Huang, and D. Wei, Layer-independent and layer-dependent nonlinear optical properties of two-dimensional GaX (X = S, Se, Te) nanosheets, Phys. Chem. Chem. Phys. **19**, 11131 (2017).
[14] H. Wang and X. Qian, Giant optical second harmonic generation in two-dimensional multiferroics, Nano Lett. **17**, 5027 (2017).
[15] C. Attaccalite, A. Nguer, E. Cannuccia, and M. Grüning, Strong second harmonic generation in SiC, ZnO, GaN two-dimensional hexagonal crystals from first-principles many-body calculations, Phys. Chem. Chem. Phys. **17**, 9533 (2015).
[16] C. Attaccalite, M. Palummo, E. Cannuccia, and M. Grüning, Second-harmonic generation in single-layer monochalcogenides: A response from first-principles real-time simulations, Phys. Rev. Mater. **3**, 074003 (2019).
[17] J. Yu, X. Kuang, J. Li, J. Zhong, C. Zeng, L. Cao, Z. Liu, Z. Zeng, Z. Luo, T. He *et al.*, Giant nonlinear optical activity in

two-dimensional palladium diselenide, Nat. Commun. **12**, 1083 (2021).
[18] G. Y. Guo and J. C. Lin, Second-harmonic generation and linear electro-optical coefficients of BN nanotubes, Phys. Rev. B **72**, 075416 (2005).
[19] G. Y. Guo, K. C. Chu, D. Wang, and C. Duan, Linear and nonlinear optical properties of carbon nanotubes from first-principles calculations, Phys. Rev. B **69**, 205416 (2004).
[20] J.-H. Song, A. J. Freeman, T. K. Bera, I. Chung, and M. G. Kanatzidis, First-principles prediction of an enhanced optical second-harmonic susceptibility of low-dimensional alkali-metal chalcogenides, Phys. Rev. B **79**, 245203 (2009).
[21] X. Lu, G. Moille, A. Rao, D. A. Westly, and K. Srinivasan, Efficient photoinduced second-harmonic generation in silicon nitride photonics, Nat. Photonics **15**, 131 (2021).
[22] A. Zumbusch, G. R. Holtom, and X. S. Xie, Three-dimensional vibrational imaging by coherent anti-Stokes Raman scattering, Phys. Rev. Lett. **82**, 4142 (1999).
[23] B. Corcoran, C. Monat, C. Grillet, D. J. Moss, B. J. Eggleton, T. P. White, L. O'Faolain, and T. F. Krauss, Green light emission in silicon through slow-light enhanced third-harmonic generation in photonic-crystal waveguides, Nat. Photonics **3**, 206 (2009).
[24] Q. Wu and X.-C. Zhang, Ultrafast electro-optic field sensors, Appl. Phys. Lett. **68**, 1604 (1996).
[25] N. Kumar, S. Najmaei, Q. Cui, F. Ceballos, P. M. Ajayan, J. Lou, and H. Zhao, Second harmonic microscopy of monolayer MoS_2, Phys. Rev. B **87**, 161403 (2013).
[26] L. M. Malard, T. V. Alencar, A. P. M. Barboza, K. F. Mak, and A. M. De Paula, Observation of intense second harmonic generation from MoS_2 atomic crystals, Phys. Rev. B **87**, 201401 (2013).
[27] D. J. Clark, V. Senthilkumar, C. T. Le, D. L. Weerawarne, B. Shim, J. I. Jang, J. H. Shim, J. Cho, Y. Sim, M.-J. Seong *et al.*, Strong optical nonlinearity of CVD-grown MoS_2 monolayer as probed by wavelength-dependent second-harmonic generation, Phys. Rev. B **90**, 121409 (2014).
[28] G. A. Wagoner, P. D. Persans, E. A. Van Wagenen, and G. M. Korenowski, Second-harmonic generation in molybdenum disulfide, J. Opt. Soc. Am. B **15**, 1017 (1998).
[29] Y. Li, Y. Rao, K. F. Mak, Y. You, S. Wang, C. R. Dean, and T. F. Heinz, Probing symmetry properties of few-layer MoS_2 and h-BN by optical second-harmonic generation, Nano Lett. **13**, 3329 (2013).
[30] K. L. Seyler, J. R. Schaibley, P. Gong, P. Rivera, A. M. Jones, S. Wu, J. Yan, D. G. Mandrus, W. Yao, and X. Xu, Electrical control of second-harmonic generation in a WSe_2 monolayer transistor, Nat. Nanotechnol. **10**, 407 (2015).
[31] L. Mennel, M. Paur, and T. Mueller, Second harmonic generation in strained transition metal dichalcogenide monolayers: MoS_2, $MoSe_2$, WS_2, and WSe_2, APL Photonics **4**, 034404 (2019).
[32] S. H. Rhim, Y. S. Kim, and A. J. Freeman, Strain-induced giant second-harmonic generation in monolayered 2 H -MoX_2 (X = S, Se, Te), Appl. Phys. Lett. **107**, 241908 (2015).
[33] C.-Y. Wang and G.-Y. Guo, Nonlinear optical properties of transition-metal dichalcogenide MX_2 (M = Mo, W; X = S, Se) monolayers and trilayers from first-principles calculations, J. Phys. Chem. C **119**, 13268 (2015).
[34] V. K. Gudelli and G.-Y. Guo, Large bulk photovoltaic effect and second-harmonic generation in few-layer pentagonal semiconductors PdS_2 and $PdSe_2$, New J. Phys. **23**, 093028 (2021).
[35] M. D. Smith and G. J. Miller, Polytypism in the Nb_3TeI_7 system, J. Alloys Compd. **281**, 202 (1998).
[36] M. D. Smith and G. J. Miller, Tantalum-niobium mixing in $Ta_{3-x}Nb_xTeI_7$ ($0 \leqslant x \leqslant 3$), Z. Anorg. Allg. Chem. **626**, 94 (2000).
[37] Y. Fang, X. Feng, D. Wang, Y. Ding, T. Lin, T. Zhai, and F. Huang, Polarization-independent second harmonic generation in 2D Van Der Waals Kagome Nb_3SeI_7 crystals, Small **19**, e2207934 (2023).
[38] H. Liu, S. Meng, and F. Liu, Screening two-dimensional materials with topological flat bands, Phys. Rev. Mater. **5**, 084203 (2021).
[39] J. Wang, Y. Fang, W. He, Q. Liu, J. Fu, X. Li, Y. Liu, B. Gao, L. Zhen, C. Xu *et al.*, Non-centrosymmetric 2D Nb_3SeI_7 with high in-plane anisotropy and optical nonlinearity, Adv. Opt. Mater. **11**, 2300031 (2023).
[40] S. Sharma, J. K. Dewhurst, and C. Ambrosch-Draxl, Linear and second-order optical response of III-V monolayer superlattices, Phys. Rev. B **67**, 165332 (2003).
[41] X. Gonze, F. Jollet, F. Abreu Araujo, D. Adams, B. Amadon, T. Applencourt, C. Audouze, J.-M. Beuken, J. Bieder, A. Bokhanchuk *et al.*, Recent developments in the ABINIT software package, Comput. Phys. Commun. **205**, 106 (2016).
[42] H. J. Monkhorst and J. D. Pack, Special points for Brillouin-zone integrations, Phys. Rev. B **13**, 5188 (1976).
[43] J. P. Perdew, K. Burke, and M. Ernzerhof, Generalized gradient approximation made simple, Phys. Rev. Lett. **77**, 3865 (1996).
[44] S. Grimme, Semiempirical GGA-type density functional constructed with a long-range dispersion correction, J. Comput. Chem. **27**, 1787 (2006).
[45] J. E. Sipe and E. Ghahramani, Nonlinear optical response of semiconductors in the independent-particle approximation, Phys. Rev. B **48**, 11705 (1993).
[46] S. Sharma and C. Ambrosch-Draxl, Second-harmonic optical response from first principles, Phys. Scr. **2004**, 128 (2004).
[47] A. D. Becke, Density-functional thermochemistry. I. The effect of the exchange-only gradient correction, J. Chem. Phys. **96**, 2155 (1992).
[48] C. Lee, W. Yang, and R. G. Parr, Development of the Colle-Salvetti correlation-energy formula into a functional of the electron density, Phys. Rev. B **37**, 785 (1988).
[49] J. Heyd, G. E. Scuseria, and M. Ernzerhof, Hybrid functionals based on a screened Coulomb potential, J. Chem. Phys. **118**, 8207 (2003).
[50] J. Heyd, G. E. Scuseria, and M. Ernzerhof, Erratum: Hybrid functionals based on a screened Coulomb potential, J. Chem. Phys. **124**, 219906 (2006).
[51] R. I. Eglitis and A. I. Popov, Systematic trends in (001) surface ab initio calculations of ABO_3 perovskites, J. Saudi Chem. Soc. **22**, 459 (2018).
[52] J. Heyd, J. E. Peralta, G. E. Scuseria, and R. L. Martin, Energy band gaps and lattice parameters evaluated with the Heyd-Scuseria-Ernzerhof screened hybrid functional, J. Chem. Phys. **123**, 174101 (2005).

[53] A. J. Garza and G. E. Scuseria, Predicting band gaps with hybrid density functionals, J. Phys. Chem. Lett. **7**, 4165 (2016).

[54] Z. H. Levine and D. C. Allan, Quasiparticle calculation of the dielectric response of silicon and germanium, Phys. Rev. B **43**, 4187 (1991).

[55] See Supplemental Material at http://link.aps.org/supplemental/10.1103/PhysRevB.109.115118 for band structures and DOS of AA-Nb_3TeI_7, AB-Nb_3SeI_7, and AA-Nb_3SBr_7; the real part of the optical dielectric function $\varepsilon(\omega)$; real and imaginary parts as well as the absolute value of the second-order susceptibility and the calculated total imaginary part decomposed into the inter- and intraband contributions of AA-Nb_3TeI_7, AB-Nb_3SeI_7, and AA-Nb_3SBr_7; the Imaginary part and absolute value of the second-order susceptibility of AB-Nb_3SeI_7 compared with the experimental result; optimized structural parameters of the four Nb_3MX_7 (M = Se, S, Te; X = I, Br) materials, which includes Ref. [37].

[56] G. J. Miller, Chemistry and properties of novel niobium cluster compounds, J. Alloys Compd. **229**, 93 (1995).

[57] J. Gao, Q. Wu, C. Persson, and Z. Wang, Irvsp: To obtain irreducible representations of electronic states in the VASP, Comput. Phys. Commun. **261**, 107760 (2021).

[58] P. Tronc, Yu. E. Kitaev, G. Wang, M. F. Limonov, A. G. Panfilov, and G. Neu, Optical selection rules for hexagonal GaN, Phys. Status Solidi B **216**, 599 (1999).

[59] L. Prussel and V. Véniard, Linear electro-optic effect in semiconductors: *Ab initio* description of the electronic contribution, Phys. Rev. B **97**, 205201 (2018).

[60] S. Bergfeld and W. Daum, Second-harmonic generation in GaAs: Experiment versus theoretical predictions of $X^{(2)}_{xyz}$, Phys. Rev. Lett. **90**, 036801 (2003).

[61] A. Narazaki, T. Hirano, J. Sasai, K. Tanaka, and K. Hirao, Second-harmonic generation in oriented cdse-nanocrystal-doped indium tin oxide film and its application to an infrared detector, MRS Proc. **607**, 421 (1999).

[62] Y. Zhao, Y. Yang, and H.-B. Sun, Nonlinear meta-optics towards applications, PhotoniX **2**, 3 (2021).

[63] E. Garmire, Nonlinear optics in daily life, Opt. Express **21**, 30532 (2013).

[64] M. Cheng, S. Wu, Z.-Z. Zhu, and G.-Y. Guo, Large second-harmonic generation and linear electro-optic effect in trigonal selenium and tellurium, Phys. Rev. B **100**, 035202 (2019).

[65] A. Cammarata, W. Zhang, P. S. Halasyamani, and J. M. Rondinelli, Microscopic origins of optical second harmonic generation in noncentrosymmetric–nonpolar materials, Chem. Mater. **26**, 5773 (2014).

[66] H. Zhang, Z. Shi, Z. Jiang, M. Yang, J. Zhang, Z. Meng, T. Hu, F. Liu, L. Cheng, Y. Xie *et al.*, Topological flat bands in 2D breathing-kagome lattice Nb_3TeCl_7, Adv. Mater. **35**, 2301790 (2023).